Solar RRL
www.solar-rrl.com

A Broadband Light-Trapping Nanostructure for InGaP/GaAs Dual-Junction Solar Cells Using Nanosphere Lithography-Assisted Chemical Etching

Shang-Hsuan Wu, Gabriel Cossio, Daniel Derkacs, and Edward T. Yu

III V-based multijunction solar cells have become the leading power generation technology for space applications due to their high power conversion ef ciency and reliable performance in extraterrestrial environments. Thinning down the absorber layers of multijunction solar cells can considerably reduce the production cost and improve their radiation hardness. Recent advances in ultrathin GaAs single-junction solar cells suggest the development of light-trapping nanostructures to increase light absorption in optically thin layers within III V-based multijunction solar cells. Herein, a novel and highly scalable nanosphere lithography-assisted chemical etching method to fabricate light-trapping nanostructures in InGaP/GaAs dual-junction solar cells is studied. Numerical models show that integrating the nanostructured Al_2O_3/Ag rear mirror signi cantly enhances the broadband absorption within the GaAs bottom cell. Results demonstrate that the light-trapping nanostructures effectively increase the short-circuit current density in GaAs bottom cells from 14.04 to 15.06 mA cm^{-2}. The simulated nanostructured InGaP/GaAs dual-junction structure shows improved current matching between the GaAs bottom cell and the InGaP top cell, resulting in 1.12x higher power conversion ef ciency. These ndings highlight the potential of light-trapping nanostructures to improve the performance of III-V-based multijunction photovoltaic systems, particularly for high-ef ciency applications in space.

1. Introduction

Multijunction solar cells provide greater power conversion ef ciency than single-junction cells by harvesting photons from the broad solar spectrum with reduced thermal losses.[1 4] Among different semiconductor materials, III V compound semiconductors are preferred in multijunction solar cells due to their outstanding optoelectronic properties such as direct bandgap, high absorption coef cient, tunable optical bandgap by compositional variation of ternary compounds, and high radiation hardness. These superior optoelectronic properties enable III V multijunction solar cells to harvest the broad solar spectrum, thus leading to a high conversion ef ciency of over 30 under unconcentrated solar illumination.[5] III V multijunction cells, particularly inverted metamorphic multijunction (IMM) solar cells,[6] have emerged as the dominant technology for photovoltaic (PV) systems powering satellites and spacecraft. However, the harsh conditions of outer space, including exposure to extraterrestrial radiation, pose challenges to the ef ciency, performance, and reliability of space PV arrays. The high-energy protons and electrons from the Earth's radiation belts and cosmic rays bombard the solar cells, leading to degradation over time.[7] These energetic particles cause the displacement of atoms within the crystal lattice of semiconductor material, thus creating defect states and increasing the number of recombination centers. The presence of radiation-induced defects adversely affects the performance of the solar cells due to the decreased minority carrier diffusion lengths and degraded charge carrier collection ef ciency. To mitigate the detrimental effects of radiation-induced defects, thinning the absorber layers of solar cells has been proposed as a strategy.[8] Thinner absorber layers minimize the diffusion length required for carriers to travel through the material, thereby limiting the impact of defects on carrier transport and improving the radiation tolerance of the solar cells. It has been reported that GaAs solar cells with an 80 nm absorber layer thickness showed no degradation in short-circuit current under high radiation exposure (10^{14} p$^+$ cm^{-2}) as compared to 74 degradation in short-circuit current density (J_{sc}) for an 800 nm absorber layer.[9] Radiation exposure data showed thicker GaAs layers in solar cells are more susceptible to radiation-induced defects in geostationary orbit, leading to signi cant performance degradation.[10 13] Moreover, thickness reduction in the absorber layer increases the power-to-weight ratio for space

S.-H. Wu, G. Cossio, E. T. Yu
Microelectronics Research Center
Chandra Family Department of Electrical and Computer Engineering
The University of Texas at Austin
Austin, TX 78758, USA
E-mail: ety@ece.utexas.edu

G. Cossio, E. T. Yu
Center for Dynamics and Control of Materials
The University of Texas at Austin
Austin, TX 78712, USA

D. Derkacs
SolAero Technologies Inc.
Albuquerque, NM 87123, USA

The ORCID identi cation number(s) for the author(s) of this article can be found under https://doi.org/10.1002/solr.202400531.

DOI: 10.1002/solr.202400531

 © 2024 Wiley-VCH GmbH

PV arrays and leads to considerable savings in material costs and epitaxial processing time.

However, thinner absorber layers will suffer from reduced absorption of incident photons near the band edge, resulting in lower J_{sc}. This incomplete absorption can be mitigated by implementing effective light-trapping schemes to suppress surface reflection loss and increase the optical path length within the absorber layer.[14,15] In recent years, signi cant progress has been made in developing light-trapping strategies for ultrathin single-junction GaAs solar cells to enhance photogenerated current. However, direct texturization of the absorber layer itself may introduce defects and increase nonradiative recombination, which can offset the bene ts of increased light absorption. To address this challenge, alternative light-trapping schemes involve nanotextured surfaces in window layers[16,17] and rear surface reflectors[18 21] for ultrathin GaAs solar cells. Effective implementation of light-trapping designs can yield a comparable photogenerated current to the conventional optically thick GaAs solar cells, despite using thinner GaAs layers. Chen et al. obtained a remarkable 19.9 ef ciency for an ultrathin solar cell based on a 205-nm-thick GaAs absorber combined with a nanostructured Ag rear mirror fabricated by soft nanoimprint lithography.[22] Sayre et al. demonstrated a rear surface nanophotonic grating to increase light absorption for an 80 nm GaAs solar cell via the displacement Talbot lithography method.[23] While many of these approaches effectively increase the absorption in the ultrathin GaAs solar cells, they often rely on expensive fabrication methods such as photolithography or nanoimprint lithography. This limitation hinders the cost-effectiveness and scalability of the process for wafer-scale cells. Moreover, although signi cant efforts have been directed toward developing nanotextured light-trapping systems for GaAs single-junction solar cells, their integration into III V compound multijunction solar cells remains limited. This gap underscores the need for a well-designed light-trapping scheme that can simultaneously achieve high conversion ef ciency and reduce the cost of monolithic epitaxy for III V multijunction solar cells.

In this study, we design and demonstrate a wafer-scale broadband light-trapping nanostructure for InGaP/GaAs dual-junction solar cells fabricated using nanosphere lithography (NSL)-assisted chemical etching. NSL enables rapid, low-cost fabrication of submicrometer nanopatterns via the self-assembled formation of a hexagonal-close-packed (HCP) monolayer of nanospheres, which serves as a patterning mask.[24] It provides a scalable and high-throughput lithography process that can be implemented for both rigid and flexible substrates.[25,26] In this fabrication approach, 500 nm polystyrene nanospheres were used to pattern a SiO_2 etch mask, and a periodic nanohole pattern was then formed by anisotropic wet chemical etching of the *p*-type AlGaAs back surface eld (BSF) layer. A periodic light-trapping Al_2O_3/Ag nanostructure array is then integrated with an InGaP/GaAs dual-junction solar cell to induce signi cantly increased absorption in the GaAs layer via a combination of Fabry Perot and guided-wave resonances, consequently increasing photocurrent density associated with light absorption in the GaAs bottom cell. The light-trapping Al_2O_3/Ag nanostructure is optimized via numerical modeling. As a result, the nanostructured device achieves higher external quantum ef ciency at long wavelengths and a corresponding improvement in short circuit current density, from 14.04 to 15.06 mA cm^{-2}. This improvement is due to increased current density associated with the lower (GaAs) subcell and consequently improved current matching. Our simulation results showed a 1.12x higher power conversion ef ciency under AM0 illumination, for nanostructured InGaP/GaAs dual-junction solar cells compared to planar InGaP/GaAs dual-junction solar cells. An InGaP/GaP test cell structure fabricated using readily scalable patterning approaches yielded a 1.07x increase in measured short-circuit current density under simulated AM0 illumination. These results indicate that light-trapping structures that can be fabricated without expensive lithographic patterning offer great promise for improving current matching in multijunction solar cells with the potential for direct application in III V-based multijunction PV systems for space applications.

2. Results and Discussion

2.1. The Light-Trapping Scheme

Multijunction III V compound solar cells, composed of distinct semiconductor subcells with different bandgaps, harness the broad spectrum of solar radiation with reduced thermal losses compared to single-junction solar cells, thereby offering enhanced power conversion ef ciency.[27,28] For multijunction solar cells, the subcells are connected in series through tunnel junctions. Therefore, current matching between the top and bottom cells is critical for optimizing device performance. Finding the optimal thickness of each subcell is crucial to maximizing optical power conversion by balancing light absorption and carrier extraction, as excessively thick layers can lead to increased carrier recombination, and extremely thin layers may limit light absorption.[29,30] Similarly, subcell thickness optimization is critically important for real-world implementation because while thicker subcells may increase optical absorption, they also increase manufacturing, decrease radiation hardness, and lower manufacturing throughput, thus negatively impacting commercial viability. Implementing a light-trapping nanostructure to increase optical absorption in the GaAs layer can improve current matching between the InGaP and GaAs subcells while minimizing manufacturing costs and increasing radiation hardness. A schematic light-trapping design for InGaP/GaAs dual-junction solar cells, along with a more conventional structure in which only a planar metal back reflector is present, is shown in **Figure** . The planar device structure (Figure 1a) with a back Ag mirror relies on specular reflection to redirect photons back into the GaAs absorber layer; however, a signi cant portion of incident light may be lost due to incomplete absorption. By strategically incorporating periodic Al_2O_3 nanostructures into the AlGaAs BSF layer, signi cant absorption enhancement can be achieved via coupling of incoming light to optical waveguide modes, wherein incident photons are effectively trapped and scattered into the semiconductor absorber layers (Figure 1b). In terms of the circular-hole geometry, it is the most accessible lithographic pattern that can be created in the NSL method. While the other nanostructures, such as pyramidal or rectangular arrays, could offer different or enhanced light-trapping effects,[15,31] the circular-hole design was selected based on a

© 2024 Wiley-VCH GmbH

2367198x, 2024, 22, Downloaded from https://onlinelibrary.wiley.com/doi/10.1002/solr.202400531 by University Of Texas Libraries, Wiley Online Library on [05/04/2025]. See the Terms and Conditions (https://onlinelibrary.wiley.com/terms-and-conditions) on Wiley Online Library for rules of use; OA articles are governed by the applicable Creative Commons License

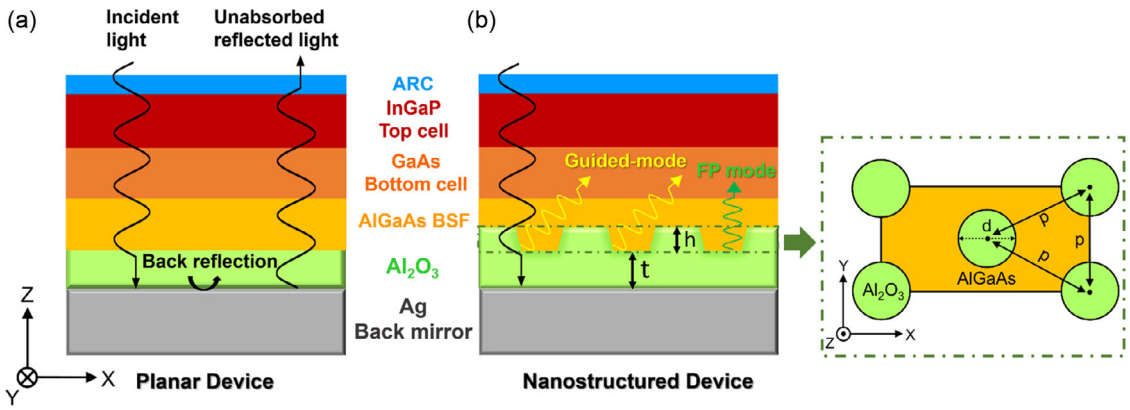

Figure 1. Schematics of InGaP/GaAs dual-junction solar cells with a) a planar Al_2O_3/Ag back reflector and b) nanostructured Al_2O_3/Ag light-trapping design. The grating geometry parameters of pitch (p), diameter (d), height (h), and the spacer thickness (t) are labeled in the gure.

combination of fabrication feasibility, scalability, and proven effectiveness in enhancing light absorption.[23] These waveguide modes enable the GaAs bottom cell, in particular, to capture longer wavelengths of sunlight, which are generally inef ciently absorbed. The Al_2O_3 nanostructures facilitate incident photons to couple to waveguide modes, which act to trap the light in horizontally propagating modes, which enable a high optical path length within the GaAs absorber layer, increasing the photocurrent to match that generated by the InGaP top cell and ensuring that both junctions contribute equally to the overall photocurrent. This balanced current generation is essential for maximizing the power output and overall performance of InGaP/GaAs dual-junction solar cells.

2.2. Optical Modeling for Light-Trapping Structures

The potential performance of light-trapping structures for current matching was determined via optical simulations based on the rigorous coupled-wave analysis method. Our device design employs two structures: rst, an Al_2O_3 dielectric spacer is placed between the metallic back contact and the BSF layer. Second, a periodic hexagonal array of nanostructures is incorporated into the BSF layer. The Al_2O_3 dielectric spacer acts to limit parasitic optical absorption in the metallic back contact due to the excitation of nonradiative plasmonic resonances. The periodic nanostructure acts as a dielectric grating to provide the necessary in-plane momentum for poorly absorbed long wavelength photons to couple into optical guided modes and as a scattering surface to increase the optical path length within the GaAs subcell. Commercially available software (RSoft, DiffractMod) was used to scan and optimize the design and fabrication-relevant variables, including the grating pitch, grating diameter, dielectric spacer thickness, and grating height. The inset of Figure 1b (green dotted line) outlines the relevant geometric variables, optical materials, and hexagonal unit cell structure utilized in our computational models.

As shown in **Figure 2**a, optical modeling was performed on nanostructures with different periodicities to nd the maxima for optical absorption within the GaAs subcell over its relevant

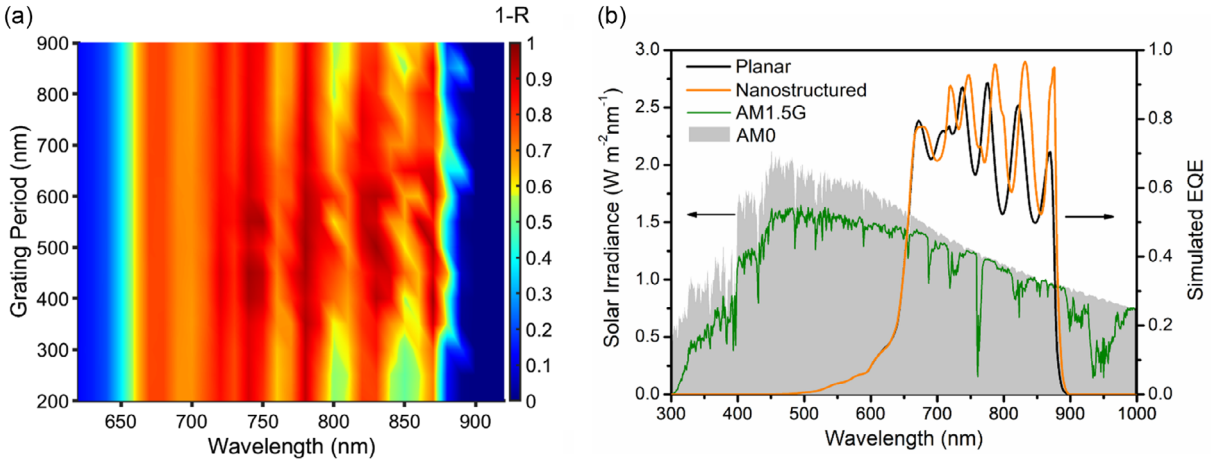

Figure 2. a) Simulated optical absorption ($1-R$) in GaAs layer as a function of incident wavelength (620–920 nm) and nanostructured grating period (200–900 nm), with d 250 nm, h 100 nm, and t 350 nm. b) AM1.5G/AM0 solar irradiance and simulated EQE spectra of GaAs bottom cells for planar, and nanostructured device structures.

© 2024 Wiley-VCH GmbH

2367198x, 2024, 22, Downloaded from https://onlinelibrary.wiley.com/doi/10.1002/solr.202400531 by University Of Texas Libraries, Wiley Online Library on [05/04/2025]. See the Terms and Conditions (https://onlinelibrary.wiley.com/terms-and-conditions) on Wiley Online Library for rules of use; OA articles are governed by the applicable Creative Commons License

wavelength range (600 900 nm). The ideal grating period for enhanced light absorption in the GaAs layer is 400 600 nm. Due to the availability of nanosphere sizes from commercial products (Polysciences Inc.), a periodicity of 500 nm was chosen for device processing. Based on the simulation results, we determined the optimal parameters for our light trapping design to be grating pitch (p) of 500 nm, grating diameter (d) of 250 nm, grating height (h) of 100 nm. The spacer thickness (t) of 350 nm was selected based on a comprehensive thickness scan ranging from 0 to 900 nm, which indicated that 350 nm provides optimal absorption (see Figure S1, Note S1, Supporting Information). Further increasing the spacer thickness beyond this value did not result in higher absorption. These speci c dimensions were chosen to balance the trade-offs between enhanced light absorption and the feasibility of fabrication. Figure 2b shows the simulated optical absorption from a conventional planar device structure (no dielectric spacer, no grating structure) and the nanostructured device with the dielectric spacer and 500 nm period grating. The nanostructured device with the added dielectric spacer and grating (orange line) shows signi cantly increased absorption at wavelengths longer than 700 nm relative to the planar device (black line). Speci cally, the planar device has an average absorption of 62 over the long-wavelength range (700 900 nm), while the nanostructured cell showed a signi - cantly higher average absorption of 70 . This enhancement is attributable to the increased optical path length of incident light within the absorber layer, multiple reflections, and scattering events induced by the nanostructures, particularly at longer wavelengths. The increase in optical absorption then also leads to a corresponding increase in short-circuit current density. To estimate the short-circuit current density (J_{sc}) of planar and nanostructured devices under AM 1.5G and AM0 illumination, we calculate J_{sc} based on the equation[23]

$$J_{sc,GaAs(InGaP} = e \int_{300nm}^{1000nm} (\quad EQE_{GaAs(InGaP} (\quad d \qquad (1)$$

where e is the elementary charge, is the photon flux per nm in the AM1.5G or AM0 spectrum, and external quantum ef ciency $(EQE)_{GaAs(InGaP)}( )$ is the external quantum ef ciency associated with the GaAs or InGaP absorber layer as a function of wavelength. The $J_{sc,GaAs(InGaP)}$ can thereby be calculated separately for the GaAs and InGaP subcells. The wavelength range was chosen to be between 300 and 1000 nm based on the bandgaps of InGaP and GaAs (1.90 and 1.42 eV, respectively). Unless otherwise speci ed, the optical power was normally incident on the solar cell structure and was 45° polarized. Based on the simulated EQE spectra of the GaAs bottom cell in Figure 2b, we see that the expected J_{sc} for the nanostructured GaAs bottom cell was enhanced by 12.3 , from 11.78 to 13.23 mA cm^{-2} under AM1.5G, and 12.1 , from 13.11 to 14.70 mA cm^{-2}, under AM0 as compared to the planar GaAs bottom cell (**Table**). Notably, while the GaAs bottom cell demonstrates enhanced absorption in the presence of nanostructures, the EQE spectra of the InGaP top cell remain unchanged between the planar and nanostructured devices (see Figure S2, Supporting Information). J_{sc} values calculated based on the simulated EQE spectra of the InGaP top cell were 14.30 and 18.22 mA cm^{-2} under AM1.5G and AM0 illumination, respectively. This is due to the high optical absorption ef ciency of InGaP within this wavelength range (300 1000 nm) and the InGaP layer being suf ciently optically thick (600 nm). These results demonstrate the great potential of light trapping as an approach to improve current matching, and thereby overall power conversion ef ciency, in InGaP/GaAs dual-junction and potentially other multijunction solar cells.

Table 1. Calculated J_{sc} values of GaAs bottom cells with planar and nanostructured Al_2O_3.

Device	Calculated J_{sc} under AM1.5G [mA cm^{-2}]	Calculated J_{sc} under AM0 [mA cm^{-2}]
Planar GaAs cell	11.78	13.11
Nanostructured GaAs cell	13.23	14.70

To further elucidate the mechanisms of the increased optical absorption in the nanostructured cell, the simulated electric eld pro les within the two cells were analyzed. **Figure 3** shows the electric eld components within the different cells when illuminated at a wavelength of 870 nm. This wavelength was chosen since both the planar and nanostructured cells share an absorption peak at 870 nm. Therefore, any changes in the electric eld pro les may help explain the large increase in absorption ef ciency of the nanostructured cell relative to the planar cell. From Figure 3a c, it can be seen that the planar cell does not support electric elds with an Ez component under 870 nm illumination, while the Ex and Ey components show oscillatory behavior. This oscillating electric eld pro le is reminiscent of a Fabry Perot resonance, which arises from the interference of vertically traveling waves after partially reflecting from the refractive index discontinuities in the semiconductor stack. In contrast to the unpatterned planar solar cell, the device with the nanostructured cell (Figure 3d f) shows a complex electric eld pro le and, importantly, a nonzero Ez component of the electric eld. Since an electric eld with a nonzero Ez component must have a wave vector component that is parallel to the XY plane, the included nanopatterned grating is horizontally scattering long-wavelength photons into guided-wave modes within the semiconductor absorber layers. The horizontally scattered photons also have an enhanced optical path length, which increases their probability of absorption. Of particular interest, the enhanced current generation from the nanostructured cell persists at all angles of incidence (Figure S3, Note S2, Supporting Information), which further demonstrates the capacity for light trapping to provide power generation bene ts in various applications which may be severely hampered by Fresnel reflection loss, such as emerging building integrated and automobile integrated PV.

2.3. Experimental Demonstration

2.3.1. Device Fabrication

Based on the numerical model, a light-trapping nanostructure with a 500 nm periodic pattern in the AlGaAs BSF layer provides optimal enhancement of broadband absorption in the GaAs

© 2024 Wiley-VCH GmbH

2367198x, 2024, 22, Downloaded from https://onlinelibrary.wiley.com/doi/10.1002/solr.202400531 by University Of Texas Libraries, Wiley Online Library on [05/04/2025]. See the Terms and Conditions (https://onlinelibrary.wiley.com/terms-and-conditions) on Wiley Online Library for rules of use; OA articles are governed by the applicable Creative Commons License

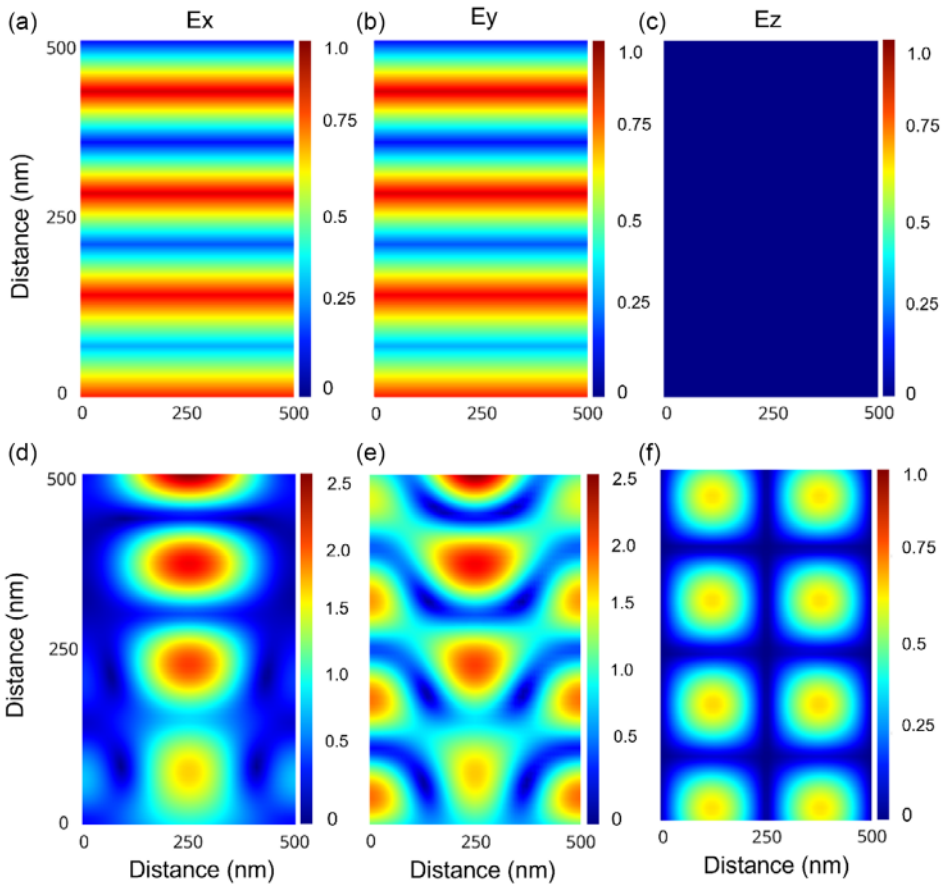

Figure 3. Electric eld components in GaAs cells illuminated at a wavelength of 870 nm for in-plane (Ex), in-plane (Ey), and out-of-plane (Ez) directions. a) Ex, b) Ey, and c) Ez elds of GaAs cells with planar structure. d) Ex, e) Ey, and f) Ez elds of GaAs cells with light-trapping structure.

bottom cell by coupling incoming light to both Fabry Perot and guided-wave resonances. The simulated EQE spectra of the InGaP top cell showed an unchanged absorption for the planar and nanostructured devices. Therefore, a simpli ed InGaP/GaAs isotype structure comprising a 600 nm InGaP lter and 500 nm GaAs absorber was prepared to study the light-trapping contribution to the GaAs bottom cells. The epitaxial layers were grown by metal-organic chemical vapor deposition (MOCVD) on a GaAs substrate in an inverted con guration with rear side grown last. A detailed description of the epitaxial layers is provided in Table S1, Supporting Information. **Figure 4** shows a schematic of the fabrication process for NSL-assisted chemical etching to create light-trapping nanostructures integrated with the InGaP/GaAs isotype structure. A 4 inch InGaP/GaAs isotype wafer was rst prepared and transferred to a drop-cast station for 500 nm polystyrene NSL using the same approach from our previous work.[32] Briefly, the colloidal solution containing polystyrene nanospheres was injected via a pipette tip to the air water interface of an aqueous reservoir and formed a HCP monolayer. The self-assembled HCP nanospheres were then deposited onto the InGaP/GaAs isotype wafer by draining the reservoir and air drying overnight at room temperature. Next, the NSL-patterned wafer was processed with an O_2 plasma etch using reactive ion etching (RIE) to reduce the diameter of the nanospheres to 100 nm. Next, a 15 nm SiO_2 hard mask layer was deposited using electron beam evaporation. The nanospheres were lifted off to form a nanopattern in the remaining SiO_2, which served as a mask for a sequential wet etch process. Selective etching of the 500 nm AlGaAs BSF layer was carried out for 75 secs using a citric acid/H_2O_2 solution[33,34] consisting of 120 g citric acid monohydrate mixed in 120 mL DI water and 15 mL 30 H_2O_2. After achieving the desired etch depth of 100 150 nm, the SiO_2 hard mask was removed by a buffered oxide etch. Al_2O_3 (350 nm) and Ag (5000 nm) were then deposited sequentially by e-beam evaporation. The isotype wafer was inverted 180°, and the Ag back surface was bonded to a rigid handling substrate coated with a low outgassing adhesive. Next, the GaAs growth substrate was mechanically thinned and chemically etched, stopping on the InGaP etch stop. Finally, HCl etching exposed the cap layer of the InGaP/GaAs isotype structure. The standard Ag-based front contact grid was deposited after the InGaP etch stop was removed. The GaAs cap was then chemically removed, exposing the InGaP lter layer, and coated with an e-beam-deposited two-layer TiO_2/Al_2O_3 antireflection coating. The wafer was mesa isolated, resulting in 12 cells wafer^{-1}, each having a physical cell area of 4.02 cm^2. The wafer was thermally annealed to promote ohmic contact formation and metal adhesion.

© 2024 Wiley-VCH GmbH

2367198x, 2024, 22, Downloaded from https://onlinelibrary.wiley.com/doi/10.1002/solr.202400531 by University Of Texas Libraries, Wiley Online Library on [05/04/2025]. See the Terms and Conditions (https://onlinelibrary.wiley.com/terms-and-conditions) on Wiley Online Library for rules of use; OA articles are governed by the applicable Creative Commons License

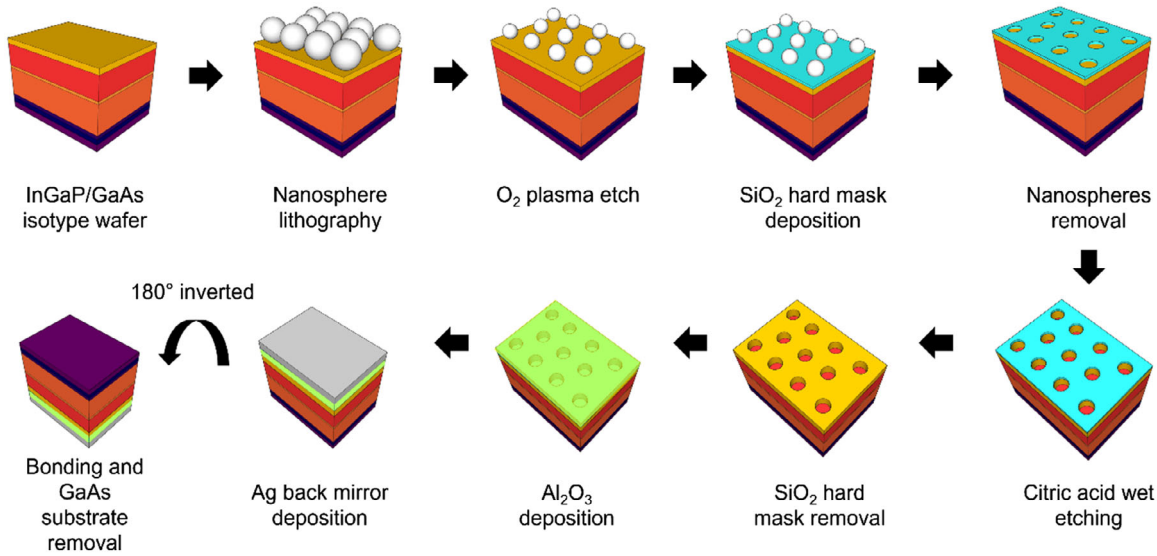

Figure 4. The fabrication process for dual-junction InGaP/GaAs solar cells incorporating a nanostructured Al_2O_3/Ag rear mirror.

To further investigate the NSL-assisted chemical wet etching process and the resulting surface morphology, we performed scanning electron microscopy (SEM) and atomic force microscopy (AFM) to characterize the etched AlGaAs BSF layer. **Figure 5**a shows an SEM image exhibiting a typical periodic pattern with an average hole diameter of 200 nm created in the AlGaAs BSF layer after 75 s of etching in citric acid/H_2O_2 solution at room temperature. The AFM image in Figure 5b shows a similar average hole diameter of 200 nm, and the corresponding AFM height pro le in Figure 5c gives an average hole depth of 120 nm. The etched hole structures showed uniform size and spacing, which can be attributed to high-quality nanosphere monolayer formation combined with good optimization of the O_2 etching process for the polystyrene nanospheres and subsequent SiO_2 etch mask formation (see Figure S4a,b, Supporting Information). Our previous work has proven that the PS nanosphere monolayer can form large single-crystal domains (2300 μm^2) and exhibit long-range order across a 158 cm^2 substrate area.[26] While there are various point and line defects in the self-assembled nanosphere arrays, these defects are deeply subwavelength and thus do not ef ciently scatter the light in the wavelength of interest. The undercut feature beneath the SiO_2 etch mask was observed during the wet etch process, and it becomes more pronounced as the etch time increases (see Figure S4c,d, Supporting Information), leading to over-etched hole dimensions and compromising the structural integrity of the features. To mitigate this issue and ensure precise control over the etched hole diameter size, we optimized a shorter etch time (75 s). The NSL-assisted chemical wet etch enables precise control in periodic nanostructures over a 4-inch wafer (see Figure S5, Supporting Information). We note that the fabrication processes employed here are all relatively fast and low cost and that the RIE step has the potential to be replaced by alternate etch processes, for example, O_2 plasma etching in a photoresist asher[35] or by deposition of core shell nanoparticles followed by a wet etch.[26]

2.3.2. Device Performance and Analysis

Figure 6a shows the measured J V characteristics of the best-performing planar and nanostructured GaAs bottom cells under

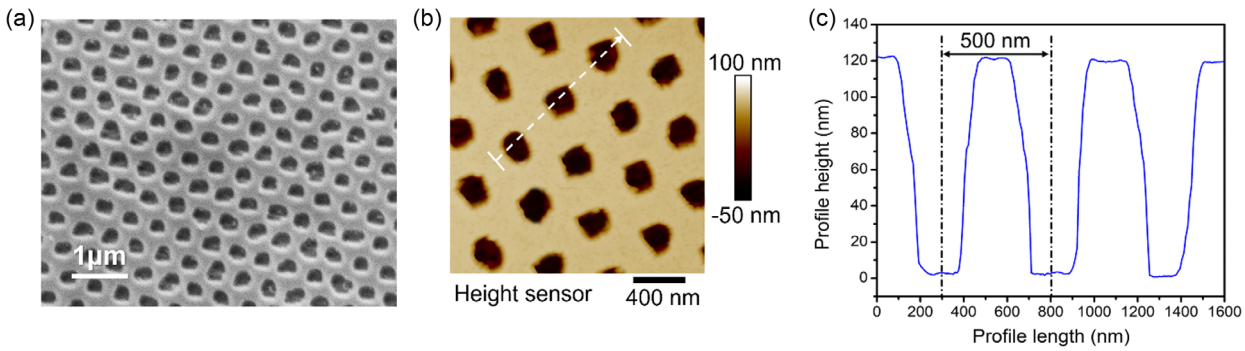

Figure 5. Surface morphology of the NSL-assisted chemical wet etched AlGaAs BSF layer. a) SEM image. b) AFM image with c) corresponding height pro le.

© 2024 Wiley-VCH GmbH

2367198x, 2024, 22, Downloaded from https://onlinelibrary.wiley.com/doi/10.1002/solr.202400531 by University Of Texas Libraries, Wiley Online Library on [05/04/2025]. See the Terms and Conditions (https://onlinelibrary.wiley.com/terms-and-conditions) on Wiley Online Library for rules of use; OA articles are governed by the applicable Creative Commons License

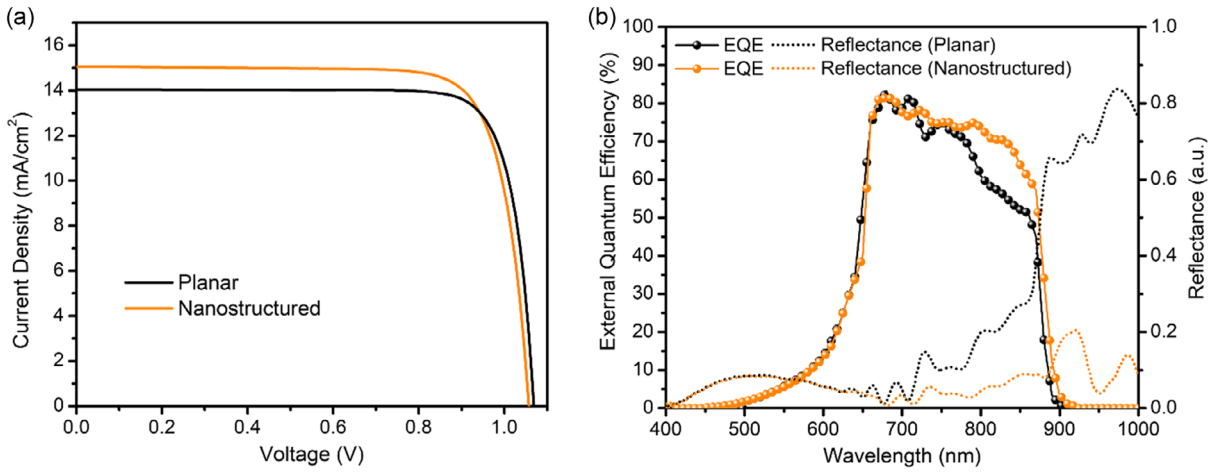

Figure 6. a) J V characteristics and b) External quantum ef ciency and specular reflectance spectra of planar and nanostructured GaAs bottom cells under AM0 illumination.

AM0 illumination. The additional J V and EQE data sets provided in Figure S6, Supporting Information, consistently demonstrate improvements in J_{sc} values and spectral response across all nanostructured devices. The PV parameters of devices are summarized in **Table 2**. Notably, the nanostructured GaAs bottom cell exhibits distinct improvement in J_{sc} 15.06 mA cm^{-2} compared to 14.04 mA cm^{-2} for the planar GaAs bottom cell. The increased J_{sc} can be ascribed to the effective light trapping and enhanced absorption from the nanostructure. However, despite the increased J_{sc}, the open-circuit voltage (V_{oc}) and ll factor (FF) in the nanostructured GaAs bottom cell exhibit slight decreases, from 1.07 to 1.05 V and 82.2 to 79.5 , respectively. The shunt resistance (R_{SH}) is t based on the slope $(dJ\ dV)^{-1}$ of the corresponding J V curves at J_{sc}. We found that the nanostructured device has a lower R_{SH} of $1.74 \times 10^3\ \Omega$ as compared to the planar device of $6.37 \times 10^4\ \Omega$. We attributed the lower V_{oc} and FF in the nanostructured device to underetching during the mesaisolation process. During this process, underetching can inadvertently create unintended conductive paths at the edges of the nanostructured areas, leading to a reduction in the overall R_{SH} of the device. A lower R_{SH} causes leakage currents that divert current from the main junction, thereby reducing both V_{oc} and FF.[36,37] Nevertheless, the power conversion ef ciency (PCE) of the nanostructured device improves from 9.03 to 9.22 . The increased J_{sc} in the nanostructured device is consistent with the enhancement in EQE (see Figure 6b). Speci cally, the nanostructured device exhibits a higher spectral response in the longer wavelength range from 700 to 900 nm than the planar device, which coincides with our simulated EQE results in Figure 2b. The slight discrepancy (5) between the integrated J_{sc} from EQE and J_{sc} obtained from the J V curve most likely originates from the mismatched external quantum ef ciency of the optically thick isotypes used to calibrate the solar simulator and the external quantum ef ciency of the optically thin devices discussed herein.[38] The specular reflectance spectra in Figure 6b show a signi cant difference between the nanostructured and planar devices, with the nanostructured device exhibiting markedly lower reflectance across the measured wavelengths. This reduction in reflectance highlights the effective light-trapping capabilities of the nanostructures. By incorporating nanostructures, the incident light is scattered into the semiconductor absorber layers rather than being reflected away, thereby enhancing the optical path length within the device. This increased optical path length boosts the photon absorption, leading to a greater generation of electron hole pairs and, subsequently, higher photocurrent. The enhanced light-trapping effect of the nanostructured device, as evidenced by the higher J_{sc} and reduced reflectance, underscores its potential to improve the overall ef ciency of solar cells by maximizing the utilization of the incident solar spectrum and, in a multijunction solar cell, allowing for improved current matching.

To further evaluate the performance of InGaP/GaAs dual-junction solar cells with light-trapping nanostructures, simulations of the J V curves for both planar and nanostructured devices were computed assuming that each subcell behaves as an ideal diode (details included in Note S3, Supporting Information) with zero series resistance. **Figure 7** shows the simulated J V curves of planar and nanostructured GaAs bottom

Table 2. PV parameters of the best planar and nanostructured GaAs bottom cells.

Device	J_{sc}[a)] [mA cm^{-2}]	J_{sc}[b)] [mA cm^{-2}]	V_{oc} [V]	FF [ ]	PCE [ ]	R_{SH} [Ω]
Planar GaAs cell	14.04	13.39	1.07	82.2	9.03	6.37×10^4
Nanostructured GaAs cell	15.06	14.33	1.05	79.5	9.22	1.74×10^3

[a)]Measured J_{sc} values from J V curves under AM0 solar simulator; [b)]Integrated J_{sc} values from the EQE measurement.

© 2024 Wiley-VCH GmbH

2367198x, 2024, 22, Downloaded from https://onlinelibrary.wiley.com/doi/10.1002/solr.202400531 by University Of Texas Libraries, Wiley Online Library on [05/04/2025]. See the Terms and Conditions (https://onlinelibrary.wiley.com/terms-and-conditions) on Wiley Online Library for rules of use; OA articles are governed by the applicable Creative Commons License

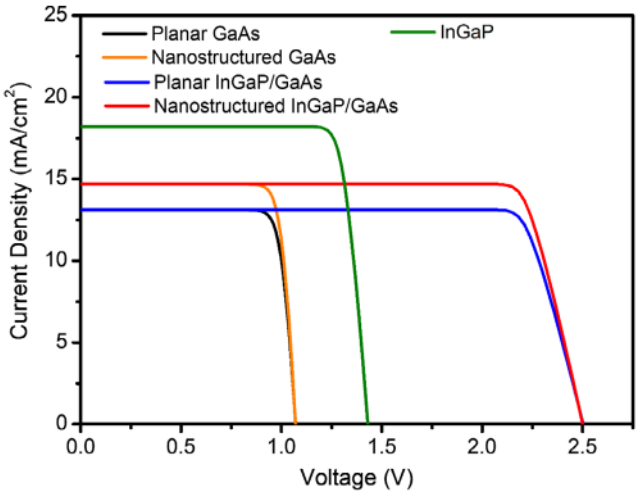

Figure 7. Simulated J V curves of planar and nanostructured GaAs bottom cells, InGaP top cell, and planar and nanostructured InGaP/GaAs dual junctions under AM0 illumination.

Table 3. Simulated PV parameters of the planar and nanostructured GaAs bottom cells and InGaP/GaAs dual junctions under AM0 illumination.

Device	J_{sc} [mA cm^{-2}]	V_{oc} [V]	FF [ ]	PCE [ ]
Planar GaAs cell	13.11	1.07	85.0	8.73
Nanostructured GaAs cell	14.70	1.07	85.0	9.79
InGaP cell	18.21	1.43	85.0	16.22
Planar InGaP/GaAs dual junction	13.11	2.50	85.0	20.39
Nanostructured InGaP/GaAs dual junction	14.70	2.50	85.0	22.87

cells, InGaP top cells, and planar and nanostructured InGaP/GaAs dual junctions under AM0 illumination. The simulated PV parameters of devices are summarized in **Table 3**. For GaAs bottom cells with an ideal FF (85) and a xed V_{oc} of 1.07 V, the nanostructured device achieves a higher J_{sc} and PCE of 14.70 mA cm^{-2} and 9.79 , respectively, compared to the planar device of 13.11 mA cm^{-2} and 8.73 . This represents a 12 improvement in performance. The J V curve of the InGaP top cell was simulated with an ideal FF (85), which showed V_{oc}, $J_{sc,}$ and PCE of 1.43 V, 18.22 mA cm^{-2}, and 16.22 , respectively. Finally, the planar and nanostructured InGaP/GaAs dual junctions were simulated, where the V_{oc} of 2.5 V is de ned as the combined value of V_{oc} of the InGaP top cells (1.43 V) and GaAs bottom cells (1.07 V). Notably, the simulated results indicate that the nanostructured device achieves better current matching with the InGaP top cell, resulting in an enhanced PCE of 22.87 in InGaP/GaAs dual-junction solar cells compared to 20.39 for the cell with a planar back contact.

3. Conclusion

In this work, a light-trapping nanostructure is designed to improve long-wavelength light absorption and consequently current matching for InGaP/GaAs dual-junction solar cells. Our numerical models demonstrate that the integration of periodic Al_2O_3/Ag nanostructures in the AlGaAs BSF layer produces a strong absorption enhancement for the GaAs bottom cell. The broadband absorption increase in the GaAs layer can be ascribed to a combination of Fabry Perot and guided-wave resonances into which incident light can be scattered by the Al_2O_3/Ag nanostructured rear mirror. Notably, the simulations indicate that an increase of 1.12x in power conversion ef ciency can be achieved in nanostructured InGaP/GaAs dual-junction solar cells, attributable to improved current matching between the GaAs bottom cells and the InGaP top cells. For experimental demonstration, we have employed a highly scalable NSL-assisted chemical etching method to fabricate light-trapping nanostructures in InGaP/GaAs dual-junction solar cells. Both J V and EQE measurements show increased J_{sc} in nanostructured GaAs bottom cells. This highlights that the NSL approach enables low-cost, large-area implementation of highly effective light-trapping nanostructures in III V-based multijunction PV systems for space applications.

4. Experimental Section

Epitaxial Growth of Semiconductor Layers: The III–V semiconductor layers were grown by MOCVD at SolAero Technologies in a Veeco E450 reactor. The layer thicknesses and doping types are provided in Table S1, Supporting Information. The epitaxial growth was conducted on GaAs substrate, consisting of InGaP etch stop, GaAs cap, InGaP lter, p^+ AlGaAs and n^+ InGaP tunnel diodes, InGap window, 500 nm GaAs homojunction as the main absorber of subcell, p^+ AlGaAs BSF, and p^{++} GaAs contact layer.

Fabrication of Nanostructured Al_2O_3/Ag Rear Mirror: First, 4 inch GaAs wafers with the epitaxial-grown InGaP/GaAs isotype structure were thoroughly cleaned using a sequential sonication process with acetone, methanol, and deionized water. Then, the wafers were immersed in water in a drop-cast container. 500 nm polystyrene nanospheres were injected at the air–water interface, creating a self-assembled monolayer of spherical particles. After that, the water was drained, allowing the HCP pattern of polystyrene spheres to deposit on the wafers. Then, the wafers were air dried at room temperature for 24 h. Next, the wafers were etched under O_2 plasma in a reactive ion etcher (Oxford Instruments) to reduce the nanosphere size. Subsequently, SiO_2 (15 nm) was deposited on the wafers using an e-beam evaporator (CHA Industries) with a base chamber pressure of 5×10^{-6} Torr and deposition rate of 1 Å s^{-1}. After that, the polystyrene spheres were lifted off the substrates using a sonication process with toluene for 10 min. The selective etching in the 500 nm AlGaAs BSF layer was carried out using a citric acid/H_2O_2 solution, which consisted of 120 g citric acid monohydrate mixed in 120 mL DI water and 15 mL 30 H_2O_2. After 75 s of the citric acid etch at room temperature, the wafers were rinsed with DI water and transferred to a buffered oxide etch for SiO_2 hard mask removal. Finally, the Al_2O_3 (350 nm) and Ag (5000 nm) were e-beam deposited sequentially to form the rear mirror.

InGaP/GaAs IMM Solar Cell Fabrication: HCl etching transferred the InGaP/GaAs tandem structure from the GaAs substrate and invertedly bonded it with a glass-handling substrate coated with epoxy. After removing the InGaP etch stop, the front contact grid of Au was deposited. Each device with an area of 4.02 cm^2 was isolated by mesa etching.

Device Characterization: The surface morphology and topography of the nanostructured AlGaAs BSF layer were investigated using SEM (Zeiss Neon 40) and AFM (Bruker Icon), respectively. J–V measurements were conducted at SolAero Technologies using a TS-Space Systems Unisim 4-zone solar simulator. The solar simulator was calibrated to the AM0 spectrum using balloon-flight-calibrated InGaP and GaAs single-junction isotypes. EQE measurements were conducted in a custom-built QE setup

© 2024 Wiley-VCH GmbH

2367198x, 2024, 22, Downloaded from https://onlinelibrary.wiley.com/doi/10.1002/solr.202400531 by University Of Texas Libraries, Wiley Online Library on [05/04/2025]. See the Terms and Conditions (https://onlinelibrary.wiley.com/terms-and-conditions) on Wiley Online Library for rules of use; OA articles are governed by the applicable Creative Commons License

using a Newport Cornerstone 260 1/4 m monochromator, Stanford Research lock-in ampli er, transimpedance ampli er, and NIST-calibrated Si, InGaAs, and Ge photodetectors. Specular reflectance was measured using a Filmetrics F20 spectrophotometer.

Optical Modeling: Simulated EQE (absorption) spectra were carried out with Synopsys, DiffractMOD model, using a 3D model based on planar and nanostructured InGaP/GaAs devices. Periodicity, diameter, and thicknesses of Al_2O_3 nanostructures were de ned as 500, 250, 100 nm, respectively. The background was set to glass (n 1.5), and the refractive index of each epitaxial layer was measured by ellipsometry. The refractive index of the Ag was obtained from DiffractMOD material database.

Supporting Information

Supporting Information is available from the Wiley Online Library or from the author.

Acknowledgements

This work was partially supported by NSF award no. CBET-2109842 and by the National Science Foundation through the Center for Dynamics and Control of Materials: an NSF MRSEC under Cooperative Agreement Nos. DMR-1720595 and DMR-2308817. The authors acknowledge the use of facilities and instrumentation supported by the National Science Foundation through the Center for Dynamics and Control of Materials: an NSF MRSEC under Cooperative Agreement Nos. DMR-1720595 and DMR-2308817. This work was performed in part at the University of Texas Microelectronics Research Center, a member of the National Nanotechnology Coordinated Infrastructure (NNCI), which was supported by the National Science Foundation (grant ECCS-2025227).

Conflict of Interest

The authors declare no conflict of interest.

Author Contributions

Shang-Hsuan Wu: Conceptualization (lead); Data curation (lead); Formal analysis (Lead); Investigation (lead); Methodology (lead); Software (lead); Validation (lead); Visualization (lead); Writing original draft (lead); Writing review & editing (lead). **Gabriel Cossio**: Conceptualization (supporting); Data curation (supporting); Formal analysis (supporting); Software (equal); Validation (supporting); Visualization (supporting); Writing original draft (supporting); Writing review & editing (supporting). **Daniel Derkacs**: Data curation (lead); Formal analysis (lead); Methodology (lead); Validation (equal); Visualization (equal); Writing original draft (supporting); Writing review & editing (supporting). **Edward T. Yu**: Conceptualization (lead); Funding acquisition (lead); Investigation (lead); Methodology (lead); Project administration (lead); Resources (lead); Software (supporting); Supervision (lead); Validation (lead); Visualization (lead); Writing original draft (equal); Writing review & editing (lead).

Data Availability Statement

The data that support the ndings of this study are available on request from the corresponding author. The data are not publicly available due to privacy or ethical restrictions.

Keywords

GaAs, III–V multijunction solar cells, light trapping, multijunction solar cells, nanosphere lithographies

Received: July 18, 2024
Revised: September 11, 2024
Published online: September 29, 2024

[1] M. Yamaguchi, T. Takamoto, A. Khan, M. Imaizumi, S. Matsuda, N. J. Ekins-Daukes, *Prog. Photovoltaics* **2005**, *13*, 125.
[2] M. S. Leite, R. L. Woo, J. N. Munday, W. D. Hong, S. Mesropian, D. C. Law, H. A. Atwater, *Appl. Phys. Lett.* **2013**, *102*, 033901.
[3] F. Dimroth, M. Grave, P. Beutel, U. Fiedeler, C. Karcher, T. N. D. Tibbits, E. Oliva, G. Siefer, M. Schachtner, A. Wekkeli, A. W. Bett, R. Krause, M. Piccin, N. Blanc, C. Drazek, E. Guiot, B. Ghyselen, T. Salvetat, A. Tauzin, T. Signamarcheix, A. Dobrich, T. Hannappel, K. Schwarzburg, *Prog. Photovoltaics* **2014**, *22*, 277.
[4] G. Oh, Y. Kim, S. J. Lee, E. K. Kim, *Sol. Energy Mater. Sol. Cells* **2020**, *207*, 110359.
[5] M. A. Green, E. D. Dunlop, M. Yoshita, N. Kopidakis, K. Bothe, G. Siefer, X. Hao, *Prog. Photovoltaics* **2024**, *32*, 3.
[6] J. F. Geisz, D. J. Friedman, J. S. Ward, A. Duda, W. J. Olavarria, T. E. Moriarty, J. T. Kiehl, M. J. Romero, A. G. Norman, K. M. Jones, *Appl. Phys. Lett.* **2008**, *93*, 123505.
[7] M. Ochoa, E. Yaccuzzi, P. Espinet-González, M. Barrera, E. Barrigón, M. L. Ibarra, Y. Contreras, J. García, E. López, M. Alurralde, C. Algora, E. Godfrin, I. Rey-Stolle, J. Plá, *Sol. Energy Mater. Sol. Cells* **2017**, *159*, 576.
[8] I. Massiot, A. Cattoni, S. Collin, *Nat. Energy* **2020**, *5*, 959.
[9] L. C. Hirst, M. K. Yakes, J. H. Warner, M. F. Bennett, K. J. Schmieder, R. J. Walters, P. P. Jenkins, *Appl. Phys. Lett.* **2016**, *109*, 033908.
[10] N. Gruginskie, F. Cappelluti, M. van Eerden, G. Bauhuis, P. Mulder, E. Vlieg, J. Schermer, *Sol. Energy Mater. Sol. Cells* **2021**, *223*, 110971.
[11] E. Yaccuzzi, S. Di Napoli, E. J. Di Liscia, S. Suárez, M. Alurralde, A. Strittmatter, J. Pla, P. Giudici, *J. Phys. D: Appl. Phys.* **2021**, *54*, 115302.
[12] J. Li, A. Aierken, Y. Liu, Y. Zhuang, X. Yang, J. H. Mo, R. K. Fan, Q. Y. Chen, S. Y. Zhang, Y. M. Huang, Q. Zhang, *Front. Phys.* **2021**, *8*, 631925.
[13] J. M. Raya-Armenta, N. Bazmohammadi, J. C. Vasquez, J. M. Guerrero, *Sol. Energy Mater. Sol. Cells* **2021**, *233*, 111379.
[14] E. T. Yu, J. van de Lagemaat, *MRS Bull.* **2011**, *36*, 424.
[15] E. Camarillo Abad, H. J. Joyce, L. C. Hirst, *Opt. Express* **2020**, *28*, 39093.
[16] S.-M. Lee, A. Kwong, D. Jung, J. Faucher, R. Biswas, L. Shen, D. Kang, M. L. Lee, J. Yoon, *ACS Nano* **2015**, *9*, 10356.
[17] D. Liang, Y. Kang, Y. Huo, Y. Chen, Y. Cui, J. S. Harris, *Nano Lett.* **2013**, *13*, 4850.
[18] W. Yang, J. Becker, S. Liu, Y.-S. Kuo, J.-J. Li, B. Landini, K. Campman, Y.-H. Zhang, *J. Appl. Phys.* **2014**, *115*, 203105.
[19] N. Vandamme, H. L. Chen, A. Gaucher, B. Behaghel, A. Lemaître, A. Cattoni, C. Dupuis, N. Bardou, J. F. Guillemoles, S. Collin, *IEEE J. Photovoltaics* **2015**, *5*, 565.
[20] M. van Eerden, G. J. Bauhuis, P. Mulder, N. Gruginskie, M. Passoni, L. C. Andreani, E. Vlieg, J. J. Schermer, *Prog. Photovoltaics* **2020**, *28*, 200.
[21] J. R. D Rozario, S. J. Polly, G. T. Nelson, S. M. Hubbard, *IEEE J. Photovoltaics* **2020**, *10*, 1681.
[22] H.-L. Chen, A. Cattoni, R. De Lépinau, A. W. Walker, O. Höhn, D. Lackner, G. Siefer, M. Faustini, N. Vandamme, J. Goffard, B. Behaghel, C. Dupuis, N. Bardou, F. Dimroth, S. Collin, *Nat. Energy* **2019**, *4*, 761.

 © 2024 Wiley-VCH GmbH

2367198x, 2024, 22, Downloaded from https://onlinelibrary.wiley.com/doi/10.1002/solr.202400531 by University Of Texas Libraries, Wiley Online Library on [05/04/2025]. See the Terms and Conditions (https://onlinelibrary.wiley.com/terms-and-conditions) on Wiley Online Library for rules of use; OA articles are governed by the applicable Creative Commons License

[23] L. Sayre, E. Camarillo Abad, P. Pearce, P. Chausse, P.-M. Coulon, P. Shields, A. Johnson, L. C. Hirst, *Prog. Photovoltaics* **2022**, *30*, 96.
[24] S.-H. Wu, G. Cossio, B. Braun, F. C. M. Wu, E. T. Yu, *Adv. Opt. Mater.* **2023**, *11*, 2202409.
[25] P. Gao, J. He, S. Zhou, X. Yang, S. Li, J. Sheng, D. Wang, T. Yu, J. Ye, Y. Cui, *Nano Lett.* **2015**, *15*, 4591.
[26] G. Cossio, R. Barbosa, B. Korgel, E. T. Yu, *Adv. Mater.* **2024**, *36*, 2309775.
[27] H. Fujii, K. Toprasertpong, Y. Wang, K. Watanabe, M. Sugiyama, Y. Nakano, *Prog. Photovoltaics* **2014**, *22*, 784.
[28] M. A. Steiner, R. M. France, J. Buencuerpo, J. F. Geisz, M. P. Nielsen, A. Pusch, W. J. Olavarria, M. Young, N. J. Ekins-Daukes, *Adv. Energy Mater.* **2021**, *11*, 2002874.
[29] A. Razi, A. Safdar, R. Irfan, *Nanomaterials* **2023**, *13*, 2985.
[30] L. Zhu, Y. Wang, X. Pan, H. Akiyama, *Opt. Express* **2022**, *30*, 35202.
[31] L. Zhu, Y. Hazama, A. Reddy, K. Watanabe, Y. Nakano, M. Sugiyama, H. Akiyama, *Prog. Photovoltaics* **2020**, *28*, 251.
[32] G. Cossio, E. T. Yu, *Nano Lett.* **2020**, *20*, 5090.
[33] G. C. DeSalvo, W. F. Tseng, J. Comas, *J. Electrochem. Soc.* **1992**, *139*, 831.
[34] J.-H. Kim, D. H. Lim, G. M. Yang, *J. Vac. Sci. Technol., B* **1998**, *16*, 558.
[35] Y. Chen, D. Shi, Y. Chen, X. Chen, J. Gao, N. Zhao, C. P. Wong, *Nanomaterials* **2019**, *9*, 605.
[36] I. M. Hamammu, K. Ibrahim, in *Proc. of the 9th Int. Conf. on Neural Information Processing, Computational Intelligence for the E-Age*, Penang, Malaysia, December **2002**.
[37] M. Raappana, T. Koikkalainen, V. Polojärvi, A. Aho, T. Aho, R. Isoaho, A. Tukiainen, M. Guina, *Sol. Energy Mater. Sol. Cells* **2021**, *226*, 111097.
[38] S. Pouladi, C. Favela, W. Wang, M. Moradnia, N.-I. Kim, S. Shervin, J. Chen, S. Sharma, G. Yang, M.-C. Nguyen, R. Choi, J. Kim, A. Fedorenko, B. Bogner, J. Bao, S. M. Hubbard, V. Selvamanickam, J.-H. Ryou, *Sol. Energy Mater. Sol. Cells* **2022**, *243*, 111791.

© 2024 Wiley-VCH GmbH

2367198x, 2024, 22, Downloaded from https://onlinelibrary.wiley.com/doi/10.1002/solr.202400531 by University Of Texas Libraries, Wiley Online Library on [05/04/2025]. See the Terms and Conditions (https://onlinelibrary.wiley.com/terms-and-conditions) on Wiley Online Library for rules of use; OA articles are governed by the applicable Creative Commons License